

Superconducting, topological and transport properties of kagome metals CsTi_3Bi_5 and RbTi_3Bi_5

Xin-Wei Yi,¹ Zheng-Wei Liao,¹ Jing-Yang You,^{2,*} Bo Gu,^{1,3,†} and Gang Su^{1,3,‡}

¹ School of Physical Sciences, University of Chinese Academy of Sciences, Beijing 100049, China

² Department of Physics, Faculty of Science, National University of Singapore, 117551, Singapore

³ Kavli Institute for Theoretical Sciences, and CAS Center for Excellence in Topological Quantum Computation, University of Chinese Academy of Sciences, Beijing 100190, China

*,†,‡ Corresponding authors

Email addresses:

phyjyy@nus.edu.sg (Jing-Yang You), gubo@ucas.ac.cn (Bo Gu), gsu@ucas.ac.cn (Gang Su)

June 26, 2023

Superconducting, topological and transport properties of kagome metals CsTi₃Bi₅ and RbTi₃Bi₅

Abstract: The recently discovered ATi₃Bi₅ (A=Cs, Rb) exhibit intriguing quantum phenomena including superconductivity, electronic nematicity, and abundant topological states, which provide promising platforms for studying kagome superconductivity, band topology, and charge orders. In this work, we comprehensively study various properties of ATi₃Bi₅ including superconductivity under pressure and doping, band topology under pressure, thermal conductivity, heat capacity, electrical resistance, and spin Hall conductivity (SHC) using first-principles calculations. Calculated superconducting transition temperature (T_c) of CsTi₃Bi₅ and RbTi₃Bi₅ at ambient pressure are about 1.85 and 1.92K. When subject to pressure, T_c of CsTi₃Bi₅ exhibits a special valley and dome shape, which arises from quasi-two-dimensional to three-dimensional isotropic compression within the context of an overall decreasing trend. Furthermore, T_c of RbTi₃Bi₅ can be effectively enhanced up to 3.09K by tuning the kagome van Hove singularities (VHSs) and flat band through doping. Pressure can also induce abundant topological surface states at the Fermi energy (E_F) and tune VHSs across E_F . Additionally, our transport calculations are in excellent agreement with recent experiments, confirming the absence of charge density wave. Notably, SHC of CsTi₃Bi₅ can reach as large as $226\hbar \cdot (e \cdot \Omega \cdot \text{cm})^{-1}$ at E_F . Our work provides a timely and detailed analysis of the rich physical properties for ATi₃Bi₅, offering valuable insights for further explorations and understandings on these intriguing superconducting materials.

keywords: CsTi₃Bi₅; RbTi₃Bi₅; Superconductivity; Electronic topology; Transport properties; Spin Hall effect.

I. INTRODUCTION

The kagome lattice composed of tiled corner-sharing triangles is a well-known two-dimensional (2D) prototype lattice, in which topological magnetism, superconductivity and frustration have been extensively studied in recent decades [1, 2]. The ideal electronic band structure of kagome lattice is characterized by flat bands, Dirac cones, quadratic band touching points and van Hove singularities (VHSs) (Fig. S1(b)). The flat bands originating from the destructive interference of wavefunctions suggest a significant correlation between electrons and can induce special negative magnetism [3], fractional quantum Hall effect [4, 5], Wigner crystallization [6], high-temperature superconductivity [7], etc. Moreover, the spin-orbit coupling (SOC) at the massless Dirac points and quadratic band touching points introduces energy gaps, which can give rise to nontrivial Z_2 topology akin to topological insulators. These gaps can even exhibit Chern gaps when subjected to magnetization [8, 9]. Fermi surface instabilities due to sublattice interference near VHS may cause different long-range charge orders and unconventional superconductivity [10–12]. Additionally, other novel physical properties, including Weyl points [13–15], giant anomalous Hall effect [16–18], quantum anomalous Hall effect [19, 20], topological superconductors [21, 22], are all intriguing research topics of kagome structure.

The recently discovered AV₃Sb₅ (A=K, Rb, Cs) kagome family exhibits various attractive properties [23]. As the pioneering examples of quasi-2D kagome superconductors, their superconducting transition temperatures (T_c) are about 1.8-2.5K under ambient pressure [24–27]. Alongside the emergence of 2×2 charge density wave (CDW) induced by VHSs with transition temperatures of about 100K [28–30], AV₃Sb₅ hosts a va-

riety of unconventional charge orders, including a nematic phase reminiscent of iron-based superconductors [31, 32], a pair density wave similar to copper-based superconductors [27], and a 4×1 CDW that induces striking phase fluctuation [33, 34]. Pressure and doping are two effective ways to manipulate the phase diagram of AV₃Sb₅. Multiple superconductivity domes simultaneously emerge intertwined with several CDW orders under pressure [30, 32, 35, 36]. Experimental substitution doping with Ti, Nb, Ta, Mo, Mn, Cr, Sn, and As in AV₃Sb₅ have been achieved, providing control over superconductivity, CDW, and nematicity [37–46]. CsV₃Sb₅, in particular, possesses both abundant non-trivial Z_2 topological surface states (TSS) and superconductivity [25, 47], and has been instrumental in resolving possible Majorana zero modes within vortex cores [48].

High-throughput density functional theory (DFT) calculations have been employed to analyze a range of compounds based on the AV₃Sb₅ prototype structure, revealing 24 dynamically stable compounds with superconductivity, abundant TSS and CDW [49]. Among them, ATi₃Bi₅ (A=Rb, Cs) compounds with enhanced T_c of about 4.8K and electronic nematicity have recently been synthesized [50–53]. Another kagome superconductor family, similar to ATi₃Bi₅, has also been predicted and awaits experimental verification [54]. The nematic order in CsV₃Sb₅ is considered as the vestige order of CDW [31]. However, the original lattice structure of ATi₃Bi₅ has been confirmed to be highly stable and devoid of CDW, as supported by calculations and thermal transport measurements [49–51, 55]. The presence of orbital-selective nematic order and intertwined superconductivity in ATi₃Bi₅ provides a new platform for exploring the multi-orbital correlation effect in nematic superconductors. In addition, exotic electronic structures have been observed in ATi₃Bi₅ using angle-resolved photoemission

spectroscopy (ARPES), including flat band, type II and type III Dirac nodal lines and Z_2 TSS [56–61]. These fascinating properties make ATi_3Bi_5 as ideal systems for investigating various kagome-related physics with reference to AV_3Sb_5 . Consequently, further investigations are imperative, particularly in examining the effects of pressure and doping on the properties of superconductivity and topology.

In this paper, we explore the superconducting and topological properties of ATi_3Bi_5 under pressure and doping by first-principles calculations. Estimated T_c of $CsTi_3Bi_5$ and $RbTi_3Bi_5$ at ambient pressure are about 1.85 and 1.92K. We observe the emergence of a special valley and dome in the T_c of $CsTi_3Bi_5$ under pressure, which is due to the crossover from quasi-2D to three-dimensional (3D) isotropic compression within the range of 10-20GPa, accompanied by a decreased background effect across all pressure ranges. Moreover, electron-phonon coupling (EPC) calculations with both a rigid band model and atomic substitution doping confirm the substantial enhancement of superconductivity in $RbTi_3Bi_5$ under doping. Additionally, pressure can lead to the presence of abundant TSS near E_F . We also discuss properties such as thermal conductivity, heat capacity, and electrical resistance, which are consistent with recent experimental findings, indicating the absence of CDW. We find that $CsTi_3Bi_5$ exhibits an intrinsic SHC of as large as $226\hbar \cdot (e \cdot \Omega \cdot \text{cm})^{-1}$ at the Fermi energy (E_F). Our findings indicate that both doping and pressure are effective means of tuning the electronic band structures and superconductivity of kagome ATi_3Bi_5 .

II. RESULTS OF $CsTi_3Bi_5$

A. Electronic Structure and van Hove Singularities

The ATi_3Bi_5 compounds exhibit a layered structure with the space group $P6/mmm$ (No. 191) as illustrated in Fig. 1(a). The central Ti_3Bi layer consists of a Ti-kagome net intertwined with a Bi triangular net, sandwiched between two Bi honeycomb layers. The triangular layers composed of A atoms are loosely bonded with the central Ti-Bi sheets. Bi atoms occupy two distinct Wyckoff positions, designated as Bi1 and Bi2, respectively. The calculated electronic band structures and partial electronic density of states (DOS) with SOC for $CsTi_3Bi_5$ are plotted in Fig. 1(b). By assigning colors to the bands based on the weights of different Ti atomic orbitals, we can identify a clear kagome flat band at about -0.4eV, VHSs at M and L points (namely VHS1 and VHS2) at about 0.2eV and massive Dirac points at K and H points contributed by $Ti-d_{x^2-y^2/xy}$ orbitals. The VHSs and flat band of $Ti-d_{x^2-y^2/xy}$ orbitals give rise to two DOS peaks at the corresponding energy levels. Notably, clear saddle features are observed in the 3D band structure near VHS2 as plotted in Fig. 1(c).

Two distinct VHSs arise from the general kagome elec-

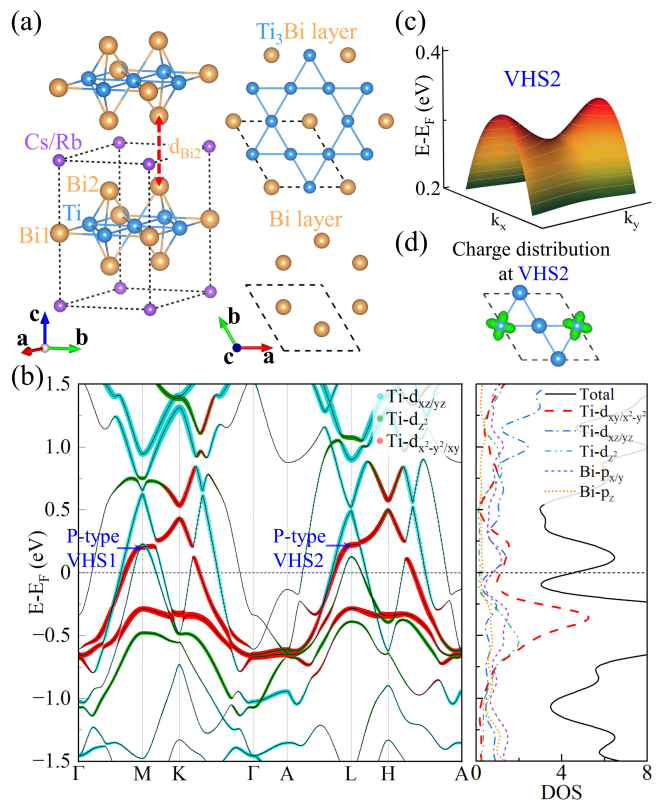


FIG. 1. **The crystal structure and electronic band structure of $CsTi_3Bi_5$.** (a) The side view of crystal structure and top views of Ti_3Bi kagome layer and Bi hexagonal layer. “ d_{Bi2} ” represents the vertical distance between Bi2 atoms in the adjacent primitive lattices, indicated by the black dotted lines. (b) Calculated electronic band structure projected by different orbitals of Ti atoms and partial density of states (DOS) with spin-orbit coupling (SOC) for $CsTi_3Bi_5$. Two kagome VHSs near the Fermi level are labeled as “VHS1” and “VHS2”, respectively. (c) 3D band structure near VHS2, with gray curves indicating constant energy contours. (d) Charge density distribution of the electronic state at VHS2 (isovalue: 0.003 e/bohr^3).

tronic bands, namely p-type and m-type VHSs, corresponding to pure and mixed sublattice characteristics at the VHS, respectively. The charge density distribution of the electronic state at the VHS2 shows pronounced in-plane d-orbital features and a p-type character as illustrated in Fig. 1(d). Unlike CsV_3Sb_5 , where all p-type VHSs are located above corresponding Dirac points, and the p-type VHS1 and VHS2 of $CsTi_3Bi_5$ lie below Dirac points in Fig. 1(b). To clarify this, we construct a tight-binding (TB) kagome model with a single orbital on each sublattice and nearest-neighboring (NN) hopping and a three-band Hamiltonian can be written as follows

$$H = \sum_{\substack{i,j \\ i \neq j}} 2t \cos(k \cdot d_{ij}) c_{i,k}^\dagger c_{j,k}, \quad (i, j = A, B, C) \quad (1)$$

where t , d_{ij} and $k = (k_x, k_y, k_z)$ represent the NN hopping parameter, NN space vector of sublattice i and

j , and wavevector of reciprocal space, respectively. A , B , and C represent three kagome sublattices. This toy kagome model produces the flat band spanning the entire Brillouin zone (BZ), VHSs at \bar{M} , Dirac point at \bar{K} , and quadratic band touching point at $\bar{\Gamma}$ as shown in Fig. S1(b) of the supplemental information (SI). By adjusting t , it becomes apparent that for $t > 0$, the p-type and m-type VHSs are located above and below the Dirac points, respectively, and the flat band resides at the top of band structure. Conversely, for $t < 0$, the bands are reversed. This observation indicates that in the kagome sublattice of CsV_3Sb_5 , all the relevant NN hopping parameters are positive, while for the Ti- $d_{x^2-y^2}/xy$ orbitals in CsTi_3Bi_5 , the NN hopping parameters exhibit negative values. P-type VHSs can induce Fermi surface instabilities [10–12], and further investigations are warranted to explore their connection with the nematic and superconducting properties in CsTi_3Bi_5 .

B. Transport properties

To gain insight into the transport properties of ATi_3Bi_5 , we calculate the temperature dependence of heat capacity C_p , thermal conductivity κ and resistance R for CsTi_3Bi_5 . These results are compared with recent experimental data as plotted in Figs. 2(a-c). The calculated results for RbTi_3Bi_5 are listed in Fig. S2. Overall, our transport calculations are in quantitative agreement with the experimental findings, demonstrating the reliability of our method. Obviously, there are no phase transition signatures in any of the transport quantities, suggesting the absence of CDW. In contrast to CsV_3Sb_5 , the total thermal conductivity $\kappa_{\text{tot,cal}}$ of CsTi_3Bi_5 is primarily governed by electronic contributions rather than phonon thermal conductivity $\kappa_{\text{phonon,cal}}$ [55]. We choose the results with the highest residual resistance ratios from Ref. [51], where the impurity concentration is the lowest in that experiment. The resistance of CsTi_3Bi_5 , as shown in Fig. S2(b), is much smaller than that of AV_3Sb_5 [25]. The calculated $R(T)/R(300\text{K})$ values align well with the experimental results at high temperatures, but underestimate the experimental data below 30K as shown in Fig. 2(c). This discrepancy arises that our resistance calculations solely consider the electron-phonon interaction and do not account for electron-electron interactions. In the experimental resistance-temperature behavior, a quadratic dependence below 30K and a linear dependence above 50K can be observed, corresponding to electron-electron and electron-phonon interactions in the normal metal, respectively. It is important to note that our calculations of the transport properties are performed on the normal phase of CsTi_3Bi_5 , and not on the superconducting phase.

In addition to the aforementioned transport properties, we also calculate the three independent components of SHC tensor, i.e. σ_{xy}^z , σ_{zx}^y , and σ_{xz}^x , as a function of the chemical potential for CsTi_3Bi_5 in Fig.2(d). The

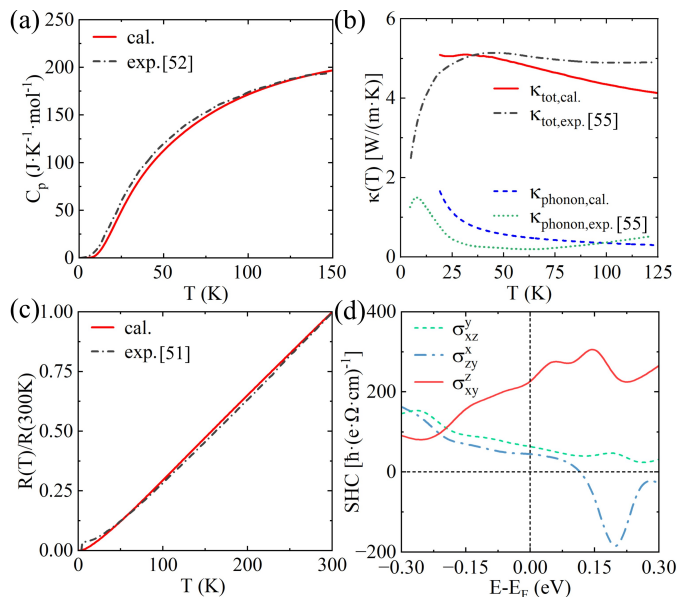


FIG. 2. **Heat capacity and transport properties of CsTi_3Bi_5 .** (a) Calculated temperature dependence of the heat capacity compared with the experiment [52]. (b) Calculated temperature dependence of the longitudinal thermal conductivity compared with the experiment [55]. (c) Calculated temperature dependence of the longitudinal electrical resistivity compared with the experiment [51]. (d) Calculated three independent components of spin Hall conductivity (SHC) tensor as a function of energy.

magnitudes of three components can reach as large as $226\hbar \cdot (\text{e} \cdot \Omega \cdot \text{cm})^{-1}$ at E_F . The large SHC comes from narrow band gap opened by large SOC [62]. The large SHC observed in CsTi_3Bi_5 implies great potential for applications in spintronic devices.

C. Superconductivity under Pressure

The superconducting T_c of CsV_3Sb_5 at pressures above 2GPa, in the absence of CDW, have been found in good agreement between EPC calculations and experimental results [63, 64]. Therefore, we can also expect DFT calculations to accurately capture the true superconductivity in ATi_3Bi_5 . The estimated T_c 's of CsTi_3Bi_5 and RbTi_3Bi_5 at ambient pressure are about 1.85 and 1.92K, respectively. The superconducting properties of both materials share remarkable similarities, so we choose CsTi_3Bi_5 as an instance to study the superconductivity under pressure.

Our calculated T_c and EPC constant λ as a function of pressure are shown in Fig. 3(a). Both values decrease in the ranges of 0-10 and 20-50 GPa, while they increase within the range of 10-20GPa, forming a unique valley and dome shape under pressure. The corresponding logarithmic average of the phonon frequency ω_{log} and the electronic DOS at the Fermi energy $N(E_F)$ are shown in Fig. 3(b). $N(E_F)$ shows an almost linear decrease

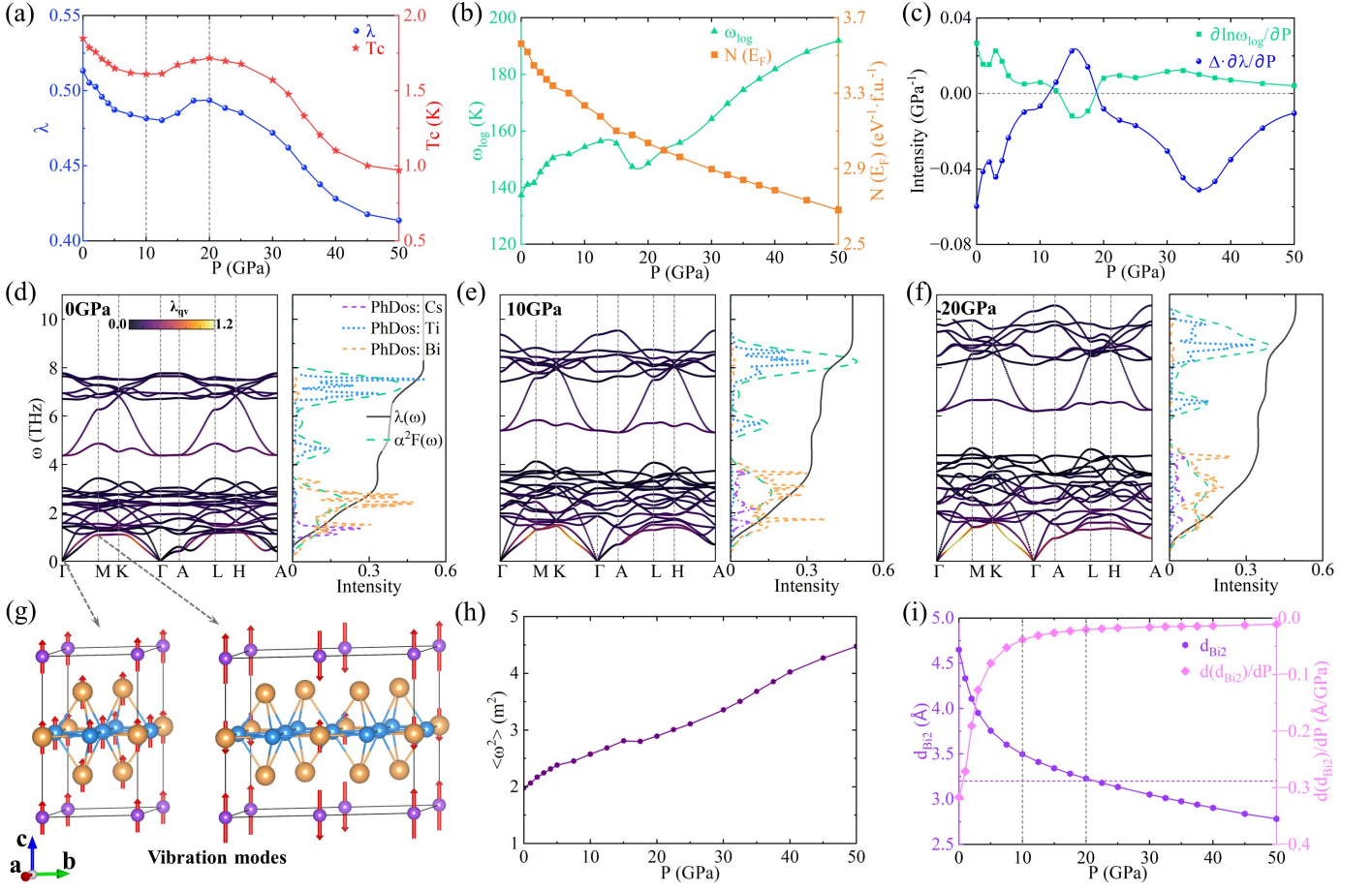


FIG. 3. **Superconducting properties of CsTi₃Bi₅ under pressure in the range of 0-50GPa.** (a) Superconducting transition temperature T_c and electron-phonon coupling (EPC) λ under pressure. (b) Logarithmic average frequency ω_{log} (K) and electronic DOS per formula unit (f.u.) at the Fermi energy $N(E_F)$ under pressure. (c) $\partial \ln \omega_{log} / \partial P$ and $\Delta \cdot \partial \lambda / \partial P$ under pressure. Phonon spectra colored by EPC strength $\lambda_{q\nu}$, projected phDOS, Eliashberg spectral function $\alpha^2 F(\omega)$, and cumulative frequency-dependent EPC $\lambda(\omega)$ at (d) 0, (e) 10, and (f) 20GPa, respectively. (g) Vibration modes at the lowest acoustic branch near Γ and M points, both of which are contributed by the vibrations along the c axis. (h) The average of square of phonon frequency $\langle \omega^2 \rangle$ under pressure. (i) d_{Bi2} denoted in Fig. 1(a) and $d(d_{Bi2})/dP$ under pressure. The horizontal dashed line indicates the Bi atomic diameter of 3.2Å.

with increasing pressure, while ω_{log} exhibits an overall increase but with a decline specifically within the 10-20GPa. It is noted that T_c is explicitly proportional to ω_{log} as described by McMillan semi-empirical formula [65, 66], $T_c = \frac{\omega_{log}}{1.2} \exp\left[-\frac{1.04(1+\lambda)}{\lambda - \mu^*(1+0.62\lambda)}\right]$, whereas the variation of T_c in CsTi₃Bi₅ shows an opposite trend compared with ω_{log} in Figs. 3(a) and (b). To address this apparent contradiction, we differentiate McMillan formula with respect to P , which gives

$$\frac{dT_c}{dP} = T_c \cdot [\partial \ln \omega_{log} / \partial P + \Delta \cdot \partial \lambda / \partial P], \quad (2)$$

$$\text{and } \Delta = \frac{1.04(1+0.38\mu^*)}{[\lambda - \mu^*(1+0.62\lambda)]^2}.$$

We calculate two terms in the brackets separately and

illustrate them in Fig. 3(c). It becomes evident that λ and ω_{log} make totally opposite contributions to $\frac{dT_c}{dP}$ across all pressure ranges. However, $\partial \ln \omega_{log} / \partial P$ is much smaller than $\Delta \cdot \partial \lambda / \partial P$. This observation explains the reason why T_c follows the same trend as λ but not ω_{log} under pressure.

The remaining question is why λ (T_c) displays a unique valley and dome shape under pressure. To shed light on this, we present the phonon spectra, projected phonon DOS (phDOS), Eliashberg spectral function $\alpha^2 F(\omega)$, and cumulative frequency-dependent EPC $\lambda(\omega)$ in Figs. 3(d-f). The corresponding results under other pressures can be found in Fig. S3. As pressure increases, the phonon frequencies (ω) within the phonon spectra noticeably increase, which is a common characteristic observed in many materials. This makes the average of the square of phonon frequency $\langle \omega^2 \rangle$ almost linearly increase under pressure as seen in Fig. 3(h). From the definition of λ ,

we have $\lambda = \frac{N(E_F)\langle I^2 \rangle}{M\langle \omega^2 \rangle}$ and $\langle \omega^2 \rangle = [\frac{2}{\lambda} \int_0^\infty \alpha^2 F(\omega) \omega d\omega]$, where $\langle I^2 \rangle$ is the mean-square electron-ion matrix element, and M is the ionic mass. It is clear that λ is proportional to $N(E_F)$ and inversely proportional to $\langle \omega^2 \rangle$. The combination of $N(E_F)$ and $\langle \omega^2 \rangle$ results in an overall decrease in λ . This mechanism accounts for the downward trend of λ and T_c within the range of 0-10 and 20-50GPa.

Upon conducting a more detailed analysis of the phonon spectra and pHDOS, we can find that the phonon spectra under pressure can be well separated into distinct high and low frequency regions. Specifically, the high-frequency region is mainly contributed by kagome Ti atoms, displaying clear kagome phonon flat band and VHSs. On the other hand, the low-frequency region primarily corresponds to the vibrational modes of Cs and Bi atoms. By separating λ into two components, namely λ_{Cs+Bi} and λ_{Ti} , we observe that λ_{Ti} gradually decreases with increasing pressure due to the aforementioned background effect, while λ_{Cs+Bi} exhibits exactly the same trend as λ , as seen in Fig. S4(a). Consequently, our analysis focuses on examining the low-frequency region within the phonon spectra in order to elucidate the trend of λ .

The total EPC λ can be decomposed into the average coupling strengths $\lambda_{\mathbf{q}\nu}$ over the BZ with $\lambda = \sum_{\mathbf{q},\nu} \lambda_{\mathbf{q}\nu}$. By coloring the phonon spectra with $\lambda_{\mathbf{q}\nu}$, we find that the high $\lambda_{\mathbf{q}\nu}$ are mainly concentrated in the lowest acoustic branch. Taking vibration modes of the lowest acoustic branch near Γ and M point as examples in Fig. 3(g), we observe that these modes primarily involve vibrations along the c-axis. Thus, based on our calculations, we can infer that the anomalous increase of λ within 10-20 GPa originates from the contributions of $\lambda_{\mathbf{q}\nu}$ associated with the out-of-plane atomic vibrations.

Next, we analyze superconductivity under pressure from a structural perspective. The vertical distance between Bi2 atoms in adjacent Ti_3Bi_5 sheets is defined as d_{Bi2} as illustrated in Fig. 1(a). Because of the quasi-2D structural features of $CsTi_3Bi_5$, d_{Bi2} is quite large, and interlayer interactions are weak. At low pressures, $d(d_{Bi2})/dP$ exhibits significant values and changes dramatically. However, as the pressure exceeds 10GPa, the rate of change in d_{Bi2} starts to slow down. Furthermore, when $P > 20$ GPa, it approaches a nearly constant value. This trend is also reflected in the ratio of the out-of-plane and in-of-plane lattice parameters c/a as depicted in Fig. S4(b). At 20GPa, d_{Bi2} becomes approximately equal to the Bi atomic diameter of 3.2Å, indicating the formation of covalent bonds among the Bi2 atoms around this pressure. These results demonstrate that the structure undergoes a quasi-2D compression below 10GPa. The weak coupling between Cs atoms and Ti_3Bi_5 sheets leads to a pronounced response of the out-of-plane lattice parameter c to applied pressure. At 10GPa, the Bi atoms of neighboring Ti_3Bi_5 sheets start to interact, leading to a significant enhancement of $\lambda_{\mathbf{q}\nu}$ associated with out-

of-plane vibrations. However, as the pressure exceeds 20GPa, the structure exhibits a 3D isotropic compression characteristic. The interaction between Bi2 atoms no longer increases but gradually decreases due to the underlying background effect mentioned earlier.

D. Topology Surface States under Pressure

Next, we explore the effect of pressure on electronic structures of $CsTi_3Bi_5$. We illustrate the calculation results at pressures of 5, 25 and 40GPa in Figs. 4(a-c), which present the electronic band structures of $CsTi_3Bi_5$ with SOC. The increased interlayer interaction under pressure profoundly impacts the band structures, leading to notable changes in the energy levels of VHSs and flat band, particularly at higher pressures. With increasing pressure, both VHSs and flat band gradually shift downwards. Remarkably, the VHSs progressively approach the vicinity of the Fermi level under pressure. Exploring the potential nematicity and other phases induced by VHSs through pressure engineering may be of significant interest.

The non-trivial TSS near Γ point of $CsTi_3Bi_5$ have been experimentally detected [51, 57, 58]. However, these TSS are approximately 0.8eV below the Fermi level, limiting their substantial effects on transport and other related properties. By examining the surface state spectra of $CsTi_3Bi_5$ under pressure in Figs. 4(d-f), we observe the emergence of multiple TSS at time-reversal invariant momenta \bar{M} and $\bar{\Gamma}$, many of which are located in proximity to the Fermi level. Under pressure, these TSS undergo slight energy shifts. Importantly, once these TSS emerge at a specific pressure, further increases in pressure do not eliminate them. The TSS in $CsTi_3Bi_5$ exhibits high tunability and sensitivity to pressure, primarily due to the dramatic changes in electronic structures.

III. SUPERCONDUCTIVITY OF $RbTi_3Bi_5$ UNDER DOPING

$RbTi_3Bi_5$ has similar electronic structure and phonon spectrum to $CsTi_3Bi_5$ as shown in Fig. S5. Therefore, we can expect $RbTi_3Bi_5$ and $CsTi_3Bi_5$ to share similar topological, transport, and superconducting properties. Since the T_c of $RbTi_3Bi_5$ is slightly higher than that of $CsTi_3Bi_5$ in our calculations, in this section, we focus on a comprehensive investigation of superconductivity in $RbTi_3Bi_5$ under doping.

Doping is an effective method to tune electronic structures and superconductivity. Extensive studies have successfully achieved doping in AV_3Sb_5 to manipulate the competition between superconductivity, CDW, and nematicity [37–46]. Notably, the concentration of Sb replacement doping with Sn in AV_3Sb_5 can reach up to 30% [40]. With reference to AV_3Sb_5 , doping in ATi_3Bi_5 is highly feasible. We first employ a rigid band model to

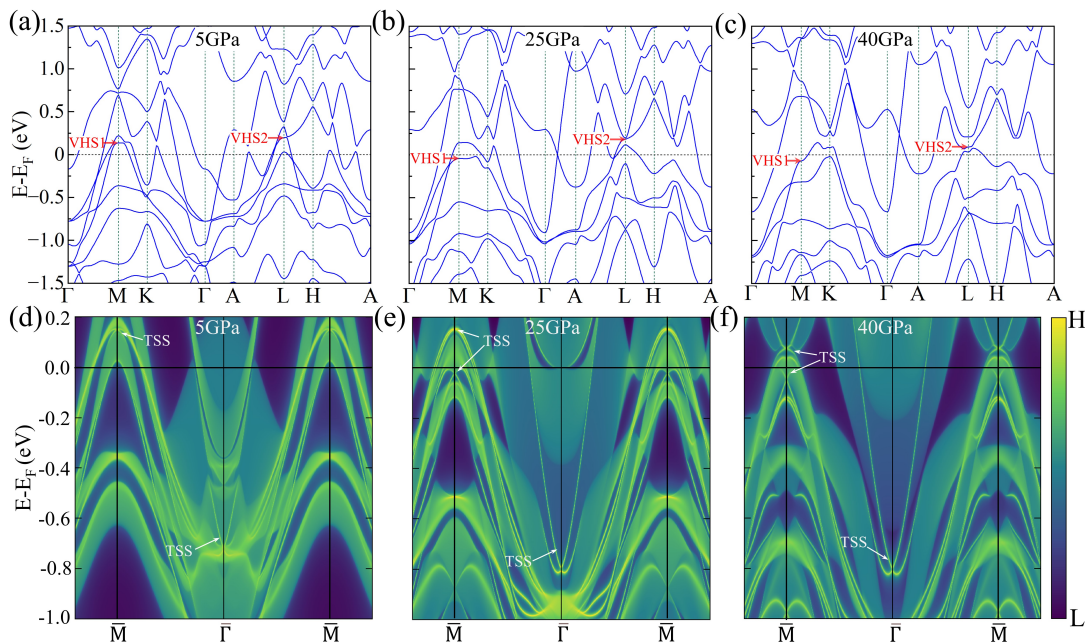


FIG. 4. **Electronic band structures and surface state spectra under pressure for CsTi₃Bi₅.** electronic band structures with SOC at (a) 5, (b) 25, and (c) 40GPa. Surface state spectra along $\bar{M} - \bar{\Gamma} - \bar{M}$ paths on the (001) plane at (d) 5, (e) 25, and (f) 40GPa. Topological surface states (TSS) are indicated with white arrows.

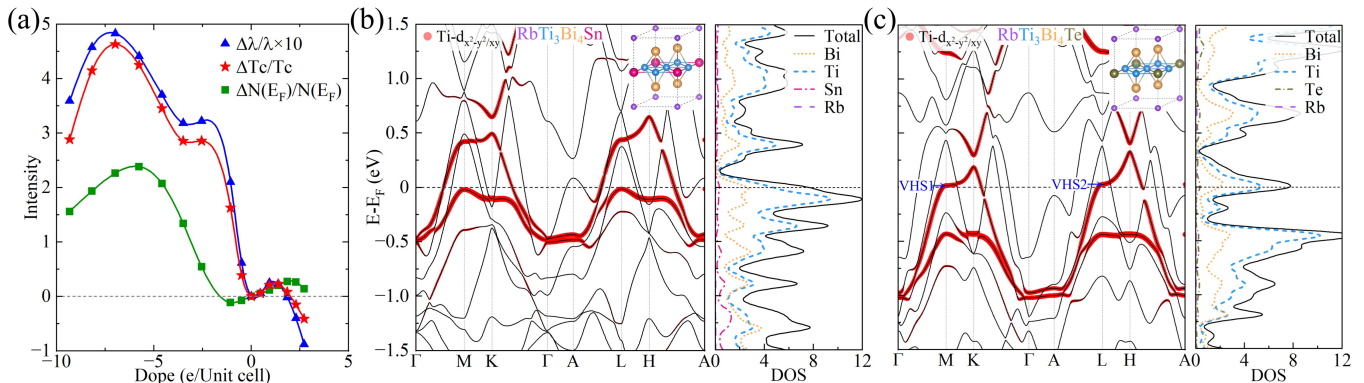


FIG. 5. **Superconductivity and electronic structures of RbTi₃Bi₅ under doping.** (a) Relative changes of λ , T_c , and $N(E_F)$ under doping using the rigid band model: $\Delta\lambda/\lambda$, $\Delta T_c/T_c$, and $\Delta N(E_F)/N(E_F)$. Calculated electronic band structures projected by Ti- $d_{x^2-y^2/xy}$ orbitals and partial DOS with SOC for (b) RbTi₃Bi₄Sn and (c) RbTi₃Bi₄Te, where the insets show the doped structures. Two kagome VHSs near the Fermi level of RbTi₃Bi₄Te are labeled as “VHS1” and “VHS2”, respectively.

analyze the effect of electron and hole doping on superconductivity. Fig. 5(a) illustrates the relative changes in λ , T_c , and $N(E_F)$ under doping. Both electron and hole doping result in enhancements of $N(E_F)$ due to the movement of VHSs and flat band towards the Fermi level. As a consequence, there are significant improvements in λ and T_c . Especially under hole doping, the highest $N(E_F)$ can be increased by nearly 2.5 times, and T_c can be increased by nearly 5 times.

In addition to the rigid band model, we also explore specific element substitution doping. Alkali metal substitutions of ATi₃Bi₅, including LiTi₃Bi₅, NaTi₃Bi₅, and KTi₃Bi₅, are found to be unstable according to our pre-

vious study [49]. Instead, we substitute one Ti or Bi atom in each unit cell of ATi₃Bi₅, corresponding to 33% Ti or 20% Bi substitution. Ti is replaced by its neighboring elements (Sc, V, Y, Zr and Nb), while Bi is substituted by Ga, Sn, Sb, Te, Pb and Bi. As illustrated in Fig. 1(a), the Bi atoms occupy two Wyckoff positions that need to be distinguished. Taking Te doping as an example, we denote the substitution of Bi2 as RbTi₃TeBi₄, and the substitution of Bi1 as RbTi₃Bi₄Te as shown in Fig. S6(a). For all doped structures, we first carry out fully geometric relaxation and self-consistent iterations in nonmagnetic (NM), ferromagnetic (FM), and antiferromagnetic (AFM) configurations as seen in Figs. S6(b)

TABLE I. **Superconductivity of doped structures for RbTi₃Bi₅**. Logarithmic average frequency ω_{log} (K), EPC $\lambda(\omega = \infty)$ and T_c of doped structures.

	RbTi ₃ Bi ₅	RbVTi ₂ Bi ₅	RbZrTi ₂ Bi ₅	RbNbTi ₂ Bi ₅	RbTi ₃ Bi ₄ Te	RbTi ₃ Bi ₄ Sb	RbTi ₃ Bi ₄ Sn	RbTi ₃ Bi ₄ Pb	RbTi ₃ Bi ₃ Sn ₂	RbTi ₃ Bi ₃ Pb ₂
λ	0.520	0.578	0.525	0.586	0.526	0.513	0.605	0.608	0.612	0.622
ω_{log} (K)	135.8	131.3	113.7	126.5	137.7	144.9	124.6	117.8	127.6	119.1
T_c (K)	1.92	2.67	2.49	2.69	2.04	1.94	2.92	2.81	3.09	3.03

and (c). The energies of the three magnetic configurations of all structures are listed in Table S1, which determines the ground state magnetic configuration. Among the doped structures with Bi substitution, the energy of the replacement of Bi2 is consistently higher than that of Bi1. This suggests that the impurity prefers to substitute the Wyckoff position of Bi1. In addition, Sc, Y, and Ga doped CsTi₃Bi₅ and RbTi₃Bi₅ all exhibit ferromagnetism, which suppresses superconductivity. Therefore, these structures are not considered in the subsequent analysis.

For these doped structures, we calculate their superconductivity as summarized in Table I. Several doped structures show varying degrees of improvement compared to the original phase's T_c . T_c of RbTi₃Bi₄Sn and RbTi₃Bi₄Pb under hole doping can be raised to around 3K. However, when increasing the doping concentration to 40% for Sn and Pb doping, denoted as RbTi₃Bi₃Sn₂ and RbTi₃Bi₃Pb₂, the results indicate that there is no significant increase in T_c 's. The electronic bands and DOS of these doped structures are given in Figs. S7-22. The kagome VHSs and flat band originating from Ti in-plane orbitals in the band structures are prominent, which undergo significant changes upon Ti doping but relatively maintain structural characteristics in the cases of Bi doping. As examples of hole and electron doping, respectively, the electronic energy bands and DOS of RbTi₃Bi₄Sn and RbTi₃Bi₄Te are plotted in Figs. 5(b) and (c). The kagome flat band of RbTi₃Bi₄Sn and the VHSs of RbTi₃Bi₄Te are shifted close to the Fermi level, and the DOS originating from the flat band and VHSs exhibit pronounced peaks near the Fermi level. This indicates a shift of the Fermi level while maintaining the character of kagome band structures. These results are consistent with the above rigid band model, demonstrating that both electron and hole doping can improve T_c by tuning the kagome electronic structures and increasing the DOS through doping. The effective modulation of superconducting properties and kagome electronic structures by doping highlights the need for further experimental investigations in this system.

IV. DISCUSSION

The two superconducting domes observed in AV₃Sb₅ at low pressures are commonly believed to be related to the competition of CDW phases [30, 32, 36]. However, theoretical analyses of the superconducting dome at around 20-40GPa are limited [67–69]. The properties

of CsTi₃Bi₅ and AV₃Sb₅ at high pressure, in the absence of CDW, are similar, suggesting that our explanations for the superconducting dome and valley in CsTi₃Bi₅ may also apply to AV₃Sb₅. Recent research attributes the appearance of high-pressure superconducting dome in AV₃Sb₅ to transitions from hexagonal to monoclinic structures [70]. In contrast, our work demonstrates that the appearance of a similar dome in CsTi₃Bi₅ does not rely on structural phase transitions but rather originates from the transition from quasi-2D to 3D compression. Further investigations are needed to explore the similarities and differences in the superconducting properties of ATi₃Bi₅ and AV₃Sb₅ under pressure.

Fu and Kane proposed that the proximity effect between the helical Dirac TSS of a topological insulator and an s-wave superconductor can induce Majorana zero modes, which can be utilized for topological quantum calculations [71]. This effect has been achieved in CsV₃Sb₅ [48]. Based on our calculations, pressure effectively induces abundant Dirac TSS near the Fermi level, whose combination with superconductivity theoretically gives rise to Majorana zero modes. This opens up another fascinating research topic for ATi₃Bi₅ and its potential for exploring topological quantum phenomena.

The interlayer van der Waals forces presented in ATi₃Bi₅ facilitate their mechanical exfoliation from the bulk structures. We explore the structural stability and superconducting properties of CsTi₃Bi₅ in the 2D monolayer limit. Three slab structures, namely CsTi₃Bi₅ (slab1), Ti₃Bi₅ (slab2) and Cs₂Ti₃Bi₅ (slab3), with different combinations of Ti₃Bi₅ layer and Cs layer are considered as seen in Fig. S23. Phonon calculations show that slab2 has minimal imaginary frequencies, while slab1 and slab3 display good dynamic stability. However, superconducting calculations reveal that their T_c 's are nearly equal to that of the bulk structures.

V. SUMMARY

In summary, we preemptively address superconducting and topological properties under pressure and doping for ATi₃Bi₅, as well as their thermal conductivity, heat capacity, electrical resistance, and SHC using first-principles calculations. The estimated T_c of CsTi₃Bi₅ presents a special down-up-down trend with increasing pressure. The two decreasing sections can be attributed to the decrease in EPC resulting from reduced electronic DOS and $\langle\omega^2\rangle$ with increasing pressure. Within this overall decreasing trend, the abnormally increased

part is associated with the sharply enhanced EPC in the low-frequency region induced by vertical vibration modes, which is related to the transition from anisotropic to isotropic compression from a structural perspective. With rigid band model calculations under doping, T_c of RbTi_3Bi_5 can increase by nearly 5 times accompanied by increased electronic DOS and EPC. Calculations for different atomic substitution structures in RbTi_3Bi_5 show improvements of T_c from 1.9 to 3.1K. Furthermore, doping and pressure serve as effective means to tune the kagome VHSs and flat band positions close to E_F . Pressure can also induce abundant Dirac-type TSS at E_F . Additionally, our transport calculations agree well with recent experimental results, indicating the absence of CDW. The resistance of CsTi_3Bi_5 shows normal metal behavior, and its thermal transport is predominantly governed by electronic contributions. The SHC of CsTi_3Bi_5 can reach up to $226\hbar \cdot (\text{e} \cdot \Omega \cdot \text{cm})^{-1}$ near the Fermi level. Our comprehensive study of the diverse physical properties in ATi_3Bi_5 underscores the need for further experimental exploration in this field.

ACKNOWLEDGMENTS

This work is supported in part by the National Key R&D Program of China (Grant No. 2018YFA0305800), the Strategic Priority Research Program of the Chinese Academy of Sciences (Grants No. XDB28000000), the National Natural Science Foundation of China (Grant

No.11834014), and the Innovation Program for Quantum Science and Technology (No. 2021ZD0301800). B.G. is supported in part by the National Natural Science Foundation of China (Grant No. c), the Chinese Academy of Sciences (Grants No. YSBR-030 and No. Y929013EA2), the Strategic Priority Research Program of Chinese Academy of Sciences (Grant No. XDB33000000), and the Beijing Natural Science Foundation (Grant No. Z190011).

CONFLICT OF INTEREST

The authors declare no competing interests.

DATA AVAILABILITY

The data that support the findings of this study are available from the corresponding authors upon reasonable request.

AUTHOR CONTRIBUTIONS

J.Y.Y., B. G. and G. S. designed and supervised the research. X.W.Y. performed theoretical calculations. All authors participated in analyzing results. X.W.Y., J.Y.Y., B.G., and G.S. prepared the figures and manuscript.

-
- [1] I. Syozi, Statistics of kagome lattice, *Prog. Theor. Phys.* **6**, 306 (1951).
- [2] J.-X. Yin, B. Lian, and M. Z. Hasan, Topological kagome magnets and superconductors, *Nature* **612**, 647 (2022).
- [3] J.-X. Yin, S. S. Zhang, G. Chang, Q. Wang, S. S. Tsirkin, Z. Guguchia, B. Lian, H. Zhou, K. Jiang, I. Belopolski, N. Shumiya, D. Multer, M. Litskevich, T. A. Cochran, H. Lin, Z. Wang, T. Neupert, S. Jia, H. Lei, and M. Z. Hasan, Negative flat band magnetism in a spin-orbit-coupled correlated kagome magnet, *Nat. Phys.* **15**, 443 (2019).
- [4] S. S. Gong, W. Zhu, and D. N. Sheng, Emergent chiral spin liquid: fractional quantum Hall effect in a kagome heisenberg model, *Sci Rep* **4**, 6317 (2014).
- [5] E. Tang, J. W. Mei, and X. G. Wen, High-temperature fractional quantum Hall states, *Phys. Rev. Lett.* **106**, 236802 (2011).
- [6] H. C. Jiang, T. Devereaux, and S. A. Kivelson, Holon Wigner crystal in a lightly doped kagome quantum spin liquid, *Phys. Rev. Lett.* **119**, 067002 (2017).
- [7] S. Miyahara, S. Kusuta, and N. Furukawa, BCS theory on a flat band lattice, *Physica C: Superconductivity* **460-462**, 1145 (2007).
- [8] K. Ohgushi, S. Murakami, and N. Nagaosa, Spin anisotropy and quantum Hall effect in the kagome lattice: Chiral spin state based on a ferromagnet, *Phys. Rev. B* **62**, R6065 (2000).
- [9] H. M. Guo and M. Franz, Topological insulator on the kagome lattice, *Phys. Rev. B* **80**, 113102 (2009).
- [10] M. L. Kiesel, C. Platt, and R. Thomale, Unconventional Fermi surface instabilities in the kagome Hubbard model, *Phys. Rev. Lett.* **110**, 126405 (2013).
- [11] M. L. Kiesel and R. Thomale, Sublattice interference in the kagome Hubbard model, *Phys. Rev. B* **86**, 121105 (2012).
- [12] W.-S. Wang, Z.-Z. Li, Y.-Y. Xiang, and Q.-H. Wang, Competing electronic orders on kagome lattices at van Hove filling, *Phys. Rev. B* **87**, 115135 (2013).
- [13] D. F. Liu, A. J. Liang, E. K. Liu, Q. N. Xu, Y. W. Li, C. Chen, D. Pei, W. J. Shi, S. K. Mo, P. Dudin, T. Kim, C. Cacho, G. Li, Y. Sun, L. X. Yang, Z. K. Liu, S. S. P. Parkin, C. Felser, and Y. L. Chen, Magnetic Weyl semimetal phase in a kagome crystal, *Science* **365**, 1282 (2019).
- [14] N. Morali, R. Batabyal, P. K. Nag, E. Liu, Q. Xu, Y. Sun, B. Yan, C. Felser, N. Avraham, and H. Beidenkopf, Fermi-arc diversity on surface terminations of the magnetic Weyl semimetal $\text{Co}_3\text{Sn}_2\text{S}_2$, *Science* **365**, 1286 (2019).
- [15] J. Y. You and Y. P. Feng, A two-dimensional kagome magnet with tunable topological phases, *Materials Today Chemistry* **30**, 101566 (2023).

- [16] E. Liu, Y. Sun, N. Kumar, L. Muchler, A. Sun, L. Jiao, S. Y. Yang, D. Liu, A. Liang, Q. Xu, J. Kroder, V. Suss, H. Borrmann, C. Shekhar, Z. Wang, C. Xi, W. Wang, W. Schnelle, S. Wirth, Y. Chen, S. T. B. Goennenwein, and C. Felser, Giant anomalous Hall effect in a ferromagnetic kagome-lattice semimetal, *Nat. Phys.* **14**, 1125 (2018).
- [17] A. K. Nayak, J. E. Fischer, Y. Sun, B. Yan, J. Karel, A. C. Komarek, C. Shekhar, N. Kumar, W. Schnelle, J. Kubler, C. Felser, and S. S. Parkin, Large anomalous Hall effect driven by a nonvanishing berry curvature in the noncollinear antiferromagnet Mn_3Ge , *Sci Adv* **2**, e1501870 (2016).
- [18] S. Nakatsuji, N. Kiyohara, and T. Higo, Large anomalous Hall effect in a non-collinear antiferromagnet at room temperature, *Nature* **527**, 212 (2015).
- [19] G. Xu, B. Lian, and S. C. Zhang, Intrinsic quantum anomalous Hall effect in the kagome lattice $Cs_2LiMn_3F_{12}$, *Phys. Rev. Lett.* **115**, 186802 (2015).
- [20] Z. Zhang, J.-Y. You, X.-Y. Ma, B. Gu, and G. Su, Kagome quantum anomalous Hall effect with high chern number and large band gap, *Phys. Rev. B* **103**, 014410 (2021).
- [21] S. Baidya, A. V. Mallik, S. Bhattacharjee, and T. Saha-Dasgupta, Interplay of magnetism and topological superconductivity in bilayer kagome metals, *Phys. Rev. Lett.* **125**, 026401 (2020).
- [22] J. Y. You, B. Gu, G. Su, and Y. P. Feng, Emergent kagome electrifies, *J. Am. Chem. Soc.* **144**, 5527 (2022).
- [23] B. R. Ortiz, L. C. Gomes, J. R. Morey, M. Winiarski, M. Bordelon, J. S. Mangum, I. W. H. Oswald, J. A. Rodriguez-Rivera, J. R. Neilson, S. D. Wilson, E. Ertekin, T. M. McQueen, and E. S. Toberer, New kagome prototype materials: discovery of KV_3Sb_5 , RbV_3Sb_5 , and CsV_3Sb_5 , *Phys. Rev. Mater.* **3**, 094407 (2019).
- [24] B. R. Ortiz, P. M. Sarte, E. M. Kenney, M. J. Graf, S. M. L. Teicher, R. Seshadri, and S. D. Wilson, Superconductivity in the Z_2 kagome metal KV_3Sb_5 , *Phys. Rev. Mater.* **5**, 034801 (2021).
- [25] B. R. Ortiz, S. M. L. Teicher, Y. Hu, J. L. Zuo, P. M. Sarte, E. C. Schueller, A. M. M. Abeykoon, M. J. Krogstad, S. Rosenkranz, R. Osborn, R. Seshadri, L. Balents, J. He, and S. D. Wilson, CsV_3Sb_5 : A Z_2 topological kagome metal with a superconducting ground state, *Phys. Rev. Lett.* **125**, 247002 (2020).
- [26] Q. Yin, Z. Tu, C. Gong, Y. Fu, S. Yan, and H. Lei, Superconductivity and normal-state properties of kagome metal RbV_3Sb_5 single crystals, *Chin. Phys. Lett.* **38**, 037403 (2021).
- [27] H. Chen, H. Yang, B. Hu, Z. Zhao, J. Yuan, Y. Xing, G. Qian, Z. Huang, G. Li, Y. Ye, S. Ma, S. Ni, H. Zhang, Q. Yin, C. Gong, Z. Tu, H. Lei, H. Tan, S. Zhou, C. Shen, X. Dong, B. Yan, Z. Wang, and H. J. Gao, Roton pair density wave in a strong-coupling kagome superconductor, *Nature* **599**, 222 (2021).
- [28] F. Du, S. Luo, B. R. Ortiz, Y. Chen, W. Duan, D. Zhang, X. Lu, S. D. Wilson, Y. Song, and H. Yuan, Pressure-induced double superconducting domes and charge instability in the kagome metal KV_3Sb_5 , *Phys. Rev. B* **103**, L220504 (2021).
- [29] H. Li, T. Zhang, T. Yilmaz, Y. Pai, C. Marvinney, A. Said, Q. Yin, C. Gong, Z. Tu, E. Vescovo, C. Nelson, R. Moore, S. Murakami, H. Lei, H. Lee, B. Lawrie, and H. Miao, Observation of unconventional charge density wave without acoustic phonon anomaly in kagome superconductors AV_3Sb_5 ($A=Rb, Cs$), *Phys. Rev. X* **11**, 031050 (2021).
- [30] K. Y. Chen, N. N. Wang, Q. W. Yin, Y. H. Gu, K. Jiang, Z. J. Tu, C. S. Gong, Y. Uwatoko, J. P. Sun, H. C. Lei, J. P. Hu, and J. G. Cheng, Double superconducting dome and triple enhancement of T_c in the kagome superconductor CsV_3Sb_5 under high pressure, *Phys. Rev. Lett.* **126**, 247001 (2021).
- [31] L. Nie, K. Sun, W. Ma, D. Song, L. Zheng, Z. Liang, P. Wu, F. Yu, J. Li, M. Shan, D. Zhao, S. Li, B. Kang, Z. Wu, Y. Zhou, K. Liu, Z. Xiang, J. Ying, Z. Wang, T. Wu, and X. Chen, Charge-density-wave-driven electronic nematicity in a kagome superconductor, *Nature* **604**, 59 (2022).
- [32] L. Zheng, Z. Wu, Y. Yang, L. Nie, M. Shan, K. Sun, D. Song, F. Yu, J. Li, D. Zhao, S. Li, B. Kang, Y. Zhou, K. Liu, Z. Xiang, J. Ying, Z. Wang, T. Wu, and X. Chen, Emergent charge order in pressurized kagome superconductor CsV_3Sb_5 , *Nature* **611**, 682 (2022).
- [33] H. Zhao, H. Li, B. R. Ortiz, S. M. L. Teicher, T. Park, M. Ye, Z. Wang, L. Balents, S. D. Wilson, and I. Zeljkovic, Cascade of correlated electron states in the kagome superconductor CsV_3Sb_5 , *Nature* **599**, 216 (2021).
- [34] J. X. Yin, Quantum dephasing of kagome superconductivity, *Sci. Bull.* **68**, 568 (2023).
- [35] C. C. Zhu, X. F. Yang, W. Xia, Q. W. Yin, L. S. Wang, C. C. Zhao, D. Z. Dai, C. P. Tu, B. Q. Song, Z. C. Tao, Z. J. Tu, C. S. Gong, H. C. Lei, Y. F. Guo, and S. Y. Li, Double-dome superconductivity under pressure in the V-based kagome metals AV_3Sb_5 ($A=Rb$ and K), *Phys. Rev. B* **105**, 094507 (2022).
- [36] F. H. Yu, D. H. Ma, W. Z. Zhuo, S. Q. Liu, X. K. Wen, B. Lei, J. J. Ying, and X. H. Chen, Unusual competition of superconductivity and charge-density-wave state in a compressed topological kagome metal, *Nat. Commun.* **12**, 3645 (2021).
- [37] Y. Zhong, J. Liu, X. Wu, Z. Guguchia, J. X. Yin, A. Mine, Y. Li, S. Najafzadeh, D. Das, r. Mielke, C., R. Khasanov, H. Luetkens, T. Suzuki, K. Liu, X. Han, T. Kondo, J. Hu, S. Shin, Z. Wang, X. Shi, Y. Yao, and K. Okazaki, Nodeless electron pairing in CsV_3Sb_5 -derived kagome superconductors, *Nature* **617**, 488 (2023).
- [38] P. Wu, Y. B. Tu, Z. Y. Wang, S. K. Yu, H. Y. Li, W. R. Ma, Z. W. Liang, Y. M. Zhang, X. C. Zhang, Z. Y. Li, Y. Yang, Z. H. Qiao, J. J. Ying, T. Wu, L. Shan, Z. J. Xiang, Z. Y. Wang, and X. H. Chen, Unidirectional electron-phonon coupling in the nematic state of a kagome superconductor, *Nat. Phys.* **10.1038/s41567-023-02031-5** (2023).
- [39] H. Yang, Z. Huang, Y. Zhang, Z. Zhao, J. Shi, H. Luo, L. Zhao, G. Qian, H. Tan, B. Hu, K. Zhu, Z. Lu, H. Zhang, J. Sun, J. Cheng, C. Shen, X. Lin, B. Yan, X. Zhou, Z. Wang, S. J. Pennycook, H. Chen, X. Dong, W. Zhou, and H.-J. Gao, Titanium doped kagome superconductor $CsV_{3-x}Ti_xSb_5$ and two distinct phases, *Sci. Bull.* **67**, 2176 (2022).
- [40] Y. M. Oey, B. R. Ortiz, F. Kaboudvand, J. Frassinetti, E. Garcia, R. Cong, S. Sanna, V. F. Mitrovic, R. Seshadri, and S. D. Wilson, Fermi level tuning and double-dome superconductivity in the kagome metal

- CsV₃Sb_{5-x}Sn_x, *Phys. Rev. Mater.* **6**, L041801 (2022).
- [41] Y. M. Oey, F. Kaboudvand, B. R. Ortiz, R. Seshadri, and S. D. Wilson, Tuning charge density wave order and superconductivity in the kagome metals KV₃Sb_{5-x}Sn_x and RbV₃Sb_{5-x}Sn_x, *Phys. Rev. Mater.* **6**, 074802 (2022).
- [42] M. Liu, T. Han, X. Hu, Y. Tu, Z. Zhang, M. Long, X. Hou, Q. Mu, and L. Shan, Evolution of superconductivity and charge density wave through Ta and Mo doping in CsV₃Sb₅, *Phys. Rev. B* **106**, L140501 (2022).
- [43] Y. Liu, C.-C. Liu, Q.-Q. Zhu, L.-W. Ji, S.-Q. Wu, Y.-L. Sun, J.-K. Bao, W.-H. Jiao, X.-F. Xu, Z. Ren, and G.-H. Cao, Enhancement of superconductivity and suppression of charge-density wave in As-doped CsV₃Sb₅, *Phys. Rev. Mater.* **6**, 124803 (2022).
- [44] X. Zhou, Y. Li, Z. Liu, J. Hao, Y. Dai, Z. Wang, Y. Yao, and H.-H. Wen, Effects of niobium doping on the charge density wave and electronic correlations in the kagome metal Cs(V_{1-x}Nb_x)₃Sb₅, *Phys. Rev. B* **107**, 125124 (2023).
- [45] G. Ding, H. Wo, Y. Gu, Y. Gu, and J. Zhao, Effect of chromium doping on superconductivity and charge density wave order in the kagome metal Cs(V_{1-x}Cr_x)₃Sb₅, *Phys. Rev. B* **106**, 235151 (2022).
- [46] Y. Liu, Y. Wang, Y. Cai, Z. Hao, X.-M. Ma, L. Wang, C. Liu, J. Chen, L. Zhou, J. Wang, S. Wang, H. He, Y. Liu, S. Cui, J. Wang, B. Huang, C. Chen, and J.-W. Mei, Doping evolution of superconductivity, charge order and band topology in hole-doped topological kagome superconductors Cs(V_{1-x}Ti_x)₃Sb₅, arXiv. 10.48550/arXiv.2110.12651 (2021).
- [47] Y. Hu, S. M. L. Teicher, B. R. Ortiz, Y. Luo, S. Peng, L. Huai, J. Ma, N. C. Plumb, S. D. Wilson, J. He, and M. Shi, Topological surface states and flat bands in the kagome superconductor CsV₃Sb₅, *Sci. Bull.* **67**, 495 (2022).
- [48] Z. Liang, X. Hou, F. Zhang, W. Ma, P. Wu, Z. Zhang, F. Yu, J. J. Ying, K. Jiang, L. Shan, Z. Wang, and X. H. Chen, Three-dimensional charge density wave and surface-dependent vortex-core states in a kagome superconductor CsV₃Sb₅, *Phys. Rev. X* **11**, 031026 (2021).
- [49] X.-W. Yi, X.-Y. Ma, Z. Zhang, Z.-W. Liao, J.-Y. You, and G. Su, Large kagome family candidates with topological superconductivity and charge density waves, *Phys. Rev. B* **106**, L220505 (2022).
- [50] H. Yang, Z. Zhao, X.-W. Yi, J. Liu, J.-Y. You, Y. Zhang, H. Guo, X. Lin, C. Shen, H. Chen, X. Dong, G. Su, and H.-J. Gao, Titanium-based kagome superconductor CsTi₃Bi₅ and topological states, arXiv. 10.48550/arXiv.2209.03840 (2022).
- [51] H. Yang, Y. Ye, Z. Zhao, J. Liu, X.-W. Yi, Y. Zhang, J. Shi, J.-Y. You, Z. Huang, B. Wang, J. Wang, H. Guo, X. Lin, C. Shen, W. Zhou, H. Chen, X. Dong, G. Su, Z. Wang, and H.-J. Gao, Superconductivity and orbital-selective nematic order in a new titanium-based kagome metal CsTi₃Bi₅, arXiv. 10.48550/arXiv.2211.12264 (2022).
- [52] D. Werhahn, B. R. Ortiz, A. K. Hay, S. D. Wilson, R. Seshadri, and D. Johrendt, The kagomé metals RbTi₃Bi₅ and CsTi₃Bi₅, *Zeitschrift für Naturforschung B* **77**, 757 (2022).
- [53] H. Li, S. Cheng, B. R. Ortiz, H. Tan, D. Werhahn, Z. Keyu, D. Johrendt, B. Yan, Z. Wang, S. D. Wilson, and I. Zeljkovic, Electronic nematicity in the absence of charge density waves in a new titanium-based kagome metal, arXiv. 10.48550/arXiv.2211.16477 (2022).
- [54] X. W. Yi, Z. W. Liao, J. Y. You, B. Gu, and G. Su, Topological superconductivity and large spin Hall effect in the kagome family Ti₆X₄ (X = Bi, Sb, Pb, Tl, and In), *iScience* **26**, 105813 (2023).
- [55] X. Chen, X. Liu, W. Xia, X. Mi, L. Zhong, K. Yang, L. Zhang, Y. Gan, Y. Liu, G. Wang, A. Wang, Y. Chai, J. Shen, X. Yang, Y. Guo, and M. He, Electrical and thermal transport properties of the kagome metals ATi₃Bi₅ (A=Rb,Cs), *Phys. Rev. B* **107**, 174510 (2023).
- [56] J. Yang, X. Yi, Z. Zhao, Y. Xie, T. Miao, H. Luo, H. Chen, B. Liang, W. Zhu, Y. Ye, J.-Y. You, B. Gu, S. Zhang, F. Zhang, F. Yang, Z. Wang, Q. Peng, H. Mao, G. Liu, Z. Xu, H. Chen, H. Yang, G. Su, H. Gao, L. Zhao, and X. J. Zhou, Observation of flat band, Dirac nodal lines and topological surface states in kagome superconductor CsTi₃Bi₅, *Nat. Commun.* accepted 10.48550/arXiv.2212.04447 (2022).
- [57] Y. Hu, C. Le, Z. Zhao, J. Ma, N. C. Plumb, M. Radovic, A. P. Schnyder, X. Wu, H. Chen, X. Dong, J. Hu, H. Yang, H.-J. Gao, and M. Shi, Non-trivial band topology and orbital-selective electronic nematicity in a new titanium-based kagome superconductor, arXiv. 10.48550/arXiv.2212.07958 (2022).
- [58] Z. Jiang, Z. Liu, H. Ma, W. Xia, Z. Liu, J. Liu, S. Cho, Y. Yang, J. Ding, J. Liu, Z. Huang, Y. Qiao, J. Shen, W. Jing, X. Liu, J. Liu, Y. Guo, and D. Shen, Flat bands, non-trivial band topology and electronic nematicity in layered kagome-lattice RbTi₃Bi₅, arXiv. 10.48550/arXiv.2212.02399 (2022).
- [59] Y. Zhou, L. Chen, X. Ji, C. Liu, K. Liao, Z. Guo, J. o. Wang, H. Weng, and G. Wang, Physical properties, electronic structure, and strain-tuned monolayer of the weak topological insulator RbTi₃Bi₅ with kagome lattice, arXiv. 10.48550/arXiv.2301.01633 (2023).
- [60] B. Liu, M. Kuang, Y. Luo, Y. Li, L. Huai, S. Peng, Z. Wei, J. Shen, B. Wang, Y. Miao, X. Sun, Z. Ou, Y. Yao, Z. Wang, and J. He, Tunable van Hove singularity without structural instability in kagome metal CsTi₃Bi₅, arXiv. 10.48550/arXiv.2212.04460 (2022).
- [61] Y. Wang, Y. Liu, Z. Hao, W. Cheng, J. Deng, Y. Wang, Y. Gu, X.-M. Ma, H. Rong, F. Zhang, S. Guo, C. Zhang, Z. Jiang, Y. Yang, W. Liu, Q. Jiang, Z. Liu, M. Ye, D. Shen, Y. Liu, S. Cui, L. Wang, C. Liu, J. Lin, Y. Liu, Y. Cai, J. Zhu, C. Chen, and J.-W. Mei, Flat band and Z₂ topology of kagome metal CsTi₃Bi₅, *Chin. Phys. Lett.* **40**, 037102 (2023).
- [62] J.-Y. You, G. Su, and Y. P. Feng, A versatile model with three-dimensional triangular lattice for unconventional transport and various topological effects, *Nat. Sci. Rev.* 10.1093/nsr/nwad114 (2023).
- [63] J.-F. Zhang, K. Liu, and Z.-Y. Lu, First-principles study of the double-dome superconductivity in the kagome material CsV₃Sb₅ under pressure, *Phys. Rev. B* **104**, 195130 (2021).
- [64] J. Si, W. Lu, Y. Sun, P. Liu, and B. Wang, Charge density wave and pressure-dependent superconductivity in the kagome metal CsV₃Sb₅: A first-principles study, *Phys. Rev. B* **105**, 024517 (2022).
- [65] W. L. McMillan, Transition temperature of strongly-coupled superconductors, *Phys. Rev.* **167**, 331 (1968).
- [66] P. B. Allen and R. C. Dynes, Transition temperature of strongly-coupled superconductors reanalyzed, *Phys. Rev. B* **12**, 905 (1975).

- [67] A. Tsirlin, P. Fertey, B. R. Ortiz, B. Klis, V. Merkl, M. Dressel, S. Wilson, and E. Uykur, Role of Sb in the superconducting kagome metal CsV_3Sb_5 revealed by its anisotropic compression, *SciPost Physics* **12**, 49 (2022).
- [68] F. Yu, X. Zhu, X. Wen, Z. Gui, Z. Li, Y. Han, T. Wu, Z. Wang, Z. Xiang, Z. Qiao, J. Ying, and X. Chen, Pressure-induced dimensional crossover in a kagome superconductor, *Phys. Rev. Lett.* **128**, 077001 (2022).
- [69] Z. Zhang, Z. Chen, Y. Zhou, Y. Yuan, S. Wang, J. Wang, H. Yang, C. An, L. Zhang, X. Zhu, Y. Zhou, X. Chen, J. Zhou, and Z. Yang, Pressure-induced reemergence of superconductivity in the topological kagome metal CsV_3Sb_5 , *Phys. Rev. B* **103**, 224513 (2021).
- [70] F. Du, R. Li, S. Luo, Y. Gong, Y. Li, S. Jiang, B. R. Ortiz, Y. Liu, X. Xu, S. D. Wilson, C. Cao, Y. Song, and H. Yuan, Superconductivity modulated by structural phase transitions in pressurized vanadium-based kagome metals, *Phys. Rev. B* **106**, 024516 (2022).
- [71] L. Fu and C. L. Kane, Superconducting proximity effect and Majorana fermions at the surface of a topological insulator, *Phys. Rev. Lett.* **100**, 096407 (2008).